Generation of top-boundary conditions for 3D ionospheric models constrained by auroral imagery and plasma flow data

J. van Irsel[1], K. A. Lynch[1], A. Mule[1], M. D. Zettergren[2]

[1]Department of Physics and Astronomy, Dartmouth College, Hanover, NH, 03755 USA
[2]Physical Sciences Department, Embry-Riddle Aeronautical University, Daytona Beach, FL, 32114 USA

Key Points:

- We provide three methods for developing ionospheric convection flow maps from limited data tracks in conjunction with auroral imagery
- These methods of generating distributed plasma flow data surrounding auroral arcs are done anisotropically using auroral imagery
- Understanding current closure in auroral arc systems requires a fully 3D perspective

Corresponding author: Jules van Irsel, `jules.van.irsel.gr@dartmouth.edu`

Abstract

Data products relating to auroral arc systems are often sparse and distributed while ionospheric simulations generally require spatially continuous maps as boundary conditions at the topside ionosphere. Fortunately, all-sky auroral imagery can provide information to fill in the gaps. This paper describes three methods for creating electrostatic plasma convection maps from multi-spectral imagery combined with plasma flow data tracks from heterogeneous sources. These methods are tailored to discrete arc structures with coherent morphologies. The first method, “reconstruction”, builds the electric potential map (from which the flow field is derived) out of numerous arc-like ridges and optimizes them against the plasma flow data. This method is designed for data from localized swarms of spacecraft distributed in both latitude and longitude. The second method, “replication”, uses a 1D across-arc flow data track and replicates these data along a determined primary and secondary arc boundary while simultaneously scaling and rotating in accordance with a zeroth-order understanding of auroral arcs. The third, “weighted replication”, performs a replication on two data tracks and calculates a weighted average between them, where the weighting is based on data track proximity. This paper shows the use of these boundary conditions in driving and assessing 3D auroral ionospheric, multi-fluid simulations.

Plain Language Summary

The aurora, or northern and southern lights, are embedded within a complicated system of interacting electric fields, magnetic fields, and charged particles, the more energetic of which produce the lights themselves by exciting the neutral atmosphere. This brings about a 3D electric current system. These currents enter and exit the atmosphere along the Earth’s magnetic field lines, and can only close their circuit between 80 and 150 km. Since auroral arcs often have sheet-like morphologies, this current closure has been studied extensively in 2D (altitude-latitude), yet not nearly as much in 3D, allowing for variations along the arcs. This paper outlines the importance of simulating auroral arc systems in 3D and thus the need for generating continuous horizontal top-boundary drivers for these simulations. This is difficult as the available data products are limited. This paper provides three methods of creating these boundary conditions using multi-color, all-sky auroral imagery in conjunction with approximately across-arc plasma flow data tracks provided by spacecraft, sounding rockets and/or radar measurements.

1 Introduction

1.1 Motivation

Measurements of auroral arc systems are often sparse, heterogeneous (i.e. multi-sourced), and distributed, yet volumetric ionospheric simulations generally require spatially continuous, two-dimensional (2D) boundary conditions on the top surface of the model space. Moreover, ionospheric plasma datasets commonly provide no more than one or perhaps two tracks of dense one-dimensional (1D) data leaving little to no information on variations along the orthogonal direction. Fortunately, information about these morphologies is something that all-sky imagery can provide.

This paper discusses the development and application of three methods for creating spatially continuous, topside ionospheric, electrostatic plasma convection maps from distributed optical data provided by all-sky, multi-spectral imagery combined with plasma flow data tracks provided by spacecraft, sounding rockets and/or radar measurements. These methodologies focus on typical sheet-like discrete auroral arc structures with high across- to along-arc gradient ratios. Furthermore, this paper shows the use of these boundary conditions in driving and assessing three-dimensional (3D) auroral ionospheric simulations.

The understanding of auroral arc scale science plays an important role in interpreting magnetosphere-ionosphere (MI) coupling, the ionospheric end of which itself involves an ongoing sequence of system science studies (Wolf, 1975; Seyler, 1990; Cowley, 2000; Lotko, 2004; Fujii et al., 2011, 2012; Marghitu, 2012; Khazanov et al., 2018; Clayton et al., 2019, 2021; Yano & Ebihara, 2021; Lynch et al., 2022; Enengl et al., 2023; Wang et al., 2024). MI coupling studies near auroral arcs demand self-consistent (per Eq. (1)), topside ionospheric maps of field-aligned current (FAC) and convection plasma flow consistent with a 3D ionospheric conductivity volume created by charged particle, auroral precipitation and sunlight. The auroral ionosphere plays a non-passive role in this coupling; even with electrostatics, the arrangement of flows and time-dependent precipitation implies evolving conductivity making the system quasi-static at best. At high latitudes, the height-integrated relation between quasi-static convective flow, FAC, and conductances is (Kelley, 2009, Eq. 8.15):

$$j_\parallel(x,y) = \Sigma_P \nabla_\perp \cdot \mathbf{E} + \mathbf{E} \cdot \nabla_\perp \Sigma_P + (\mathbf{E} \times \mathbf{b}) \cdot \nabla_\perp \Sigma_H, \tag{1}$$

where $j_{\|}$ is the ionospheric topside map of FAC orthogonal to the local magnetic field, $\Sigma_{P,H}$ are the height-integrated Pedersen and Hall conductivities, i.e. conductances, $\mathbf{E}$ is the ionospheric electric field, and $\mathbf{b} = \mathbf{B}/B$ is the magnetic field direction. This explains, in the absence of induction, how magnetospheric currents and convection patterns couple to the ionosphere given height-integrated conductivity maps using the ionospheric Ohm's law and current continuity. Integrating out altitudinal effects, however, can hide significant information regarding auroral arc systems. Altitude dependent, finite recombination times, together with plasma transport, can produce 3D electron density structures providing an auroral precipitation hysteresis in conductance maps. Moreover, the 3D conductivity volume is highly sensitive to auroral precipitation by means of impact ionization, as the precipitation energy spectra determine ionization rate profiles that are altitude dependent (Fang et al., 2008, 2010). Altitudinal effects aside, the third term in Eq. (1) is typically also ignored in sheet-like assumptions. In some cases, where the ionosphere is modelled as a slab of constant conductance, the second term is ignored as well. For proper understanding of MI coupling, it is important to study the full 3D system when looking at FAC closure influenced by auroral precipitation that is both geophysical and self-consistent with plasma convection. Hence, we need ionospheric simulations that look at the full, 3D current continuity equation, an engagement that requires spatially continuous top-boundary input maps.

Both Eq. (1) and topics discussed in this paper deal with self-consistency, not causal relationships, when finding solutions to auroral current continuity. Hypotheses can be made on causality through intuition, but cannot be proven within the framework outlined in this paper.

1.2 Background

The problem of extrapolating convection flow into continuous maps is not new. Nicolls et al. (2014) undertake the mapping (or "imaging") of electric field distributions using line-of-sight (LOS) plasma flow measurements from a single, multibeam incoherent scatter radar (ISR). They outline a regularized least-squares fitting algorithm which takes direct LOS flow measurements, along with their measurement error, and produces an electric potential map. This is a difficult feat in that a single LOS measurement only carries information on one component of the electric field; multistatic beams are required to discover information about the full vector field without regularization assumptions.

Part of their regularization minimizes the mean squared curvature of the potential field (with an adjustable tailoring parameter) which results in the smoothest possible solutions and minimizes gradients isotropically, something not well suited near sheet-like auroral arcs with zeroth order across-arc conductance gradients.

Bristow et al. (2016) approach a similar problem but with multiple HF radars by using Local Divergence-Free Fitting (LDFF), as opposed to a global divergence-free constraint. They impose the local constraint of divergence-free plasma convection and treat this in the same way the recomposition of two LOS measurements constraint is treated. This achieves larger gradients, and in turn higher spatial resolution; however, this method does not take into account auroral boundaries that will factor significantly into current continuity near the arc and associated flows/potentials.

Laundal et al. (2022) describe methodology for the "Local mapping of polar ionospheric electrodynamics" (Lompe). This is an assimilative tool that gathers relatively dense, heterogeneous observational data and performs a regional mapping of the electrodynamics in the polar ionosphere. They use Spherical Elementary Current Systems (SECS, Amm, 1997) instead of the more global spherical bases used by other assimilative tools like the Kamide-Richmond-Matsushita (KRM, Kamide et al., 1981) and the Assimilative Mapping of Ionospheric Electrodynamics (AMIE, Richmond & Kamide, 1988) methods, which allows more flexibility when it comes to spatial scales. Lompe, in its default configuration, uses smooth background conductance patterns derived from a statistical model and does not fully capture the variations due to arc-scale structures.

For ideal, sheet-like auroral arcs, often only the first term in Eq. (1) is considered. In order to address the zeroth order effects of strong and anisotropic conductivity gradients in the vicinity of auroral arcs, this paper presents, first, a formalization of techniques developed during the Phase A Concept Study Report (CSR) for the Auroral Reconstruction CubeSwarm (ARCS) mission proposal (Lynch et al., 2024; Erlandson et al., 2024) and second, an extension of techniques developed by Clayton et al. (2019, 2021). We provide methodologies for the continuous mapping of plasma flow data tracks which focus on auroral physical and gradient scale lengths, and discrete sheet-like morphologies, and we use such maps as top-boundary drivers for 3D ionospheric simulations.

Section 2 describes the reconstruction, replication, and weighted replication methodology along with example usages of each one. Section 3 outlines and compares two 3D auroral multi-fluid simulations driven by the plasma flow maps derived by the replication method in Section 2.2. In section 4 we discuss our results and provide cautionary remarks, and in Section 5 we conclude this work and outline how these tools can be used in the future.

2 Methodologies

We outline three methods for developing continuous topside ionospheric plasma flow maps from limited remote sensed or in situ flow data tracks collected in conjunction with auroral imagery. Section 2.1 outlines the first methodology, coined "reconstruction", which stems from the science section in the ARCS CSR (Lynch et al., 2024). This report proposes an arrayed, localized swarm of spacecraft spanning both multiple latitudes *and* longitudes, i.e. a "CubeSwarm". The reconstruction method prioritizes accurate flow representation interior to the swarm array and builds the flow map using a pseudo-basis set of electric potential ridges, ensuring electrostatic flow. These ridges follow some definition of a single auroral arc boundary determined using morphological features of all-sky, multi-spectral imagery or, in some cases, maps of FAC from the swarm itself. The left column of Figure 1 outlines the geographical context of the Observing System Simulation Experiment (OSSE) used in Lynch et al. (2024) to demonstrate the reconstruction technique. This OSSE is interpolated with a virtual spacecraft swarm to provide multipoint, hypothesized in situ plasma flow data.

The second method, "replication", outlined in Section 2.2, extends related methodology used by Clayton et al. (2019, 2021) who use data from the Isinglass sounding rocket campaign in conjunction with imagery from the UAF Geophysical Institute's Poker Flat Digital All-Sky Camera (DASC) (Conde et al., 2001). This method makes use of plasma flow data from a single auroral arc crossing, whether from a sounding rocket (Clayton et al., 2019, 2021), spacecraft (Archer et al., 2017), or ISR (Kaeppler et al., 2023). In the present work, the data are replicated, scaled, and rotated in accordance with *two* auroral arc boundaries, again, determined through all-sky imagery features. After this, electrostatic enforcing is applied. The right column of Figure 1 shows the geographical context of the simulation used to demonstrate the replication technique.

The third method, a permutation of the second, named "weighted replication", is outlined in Section 2.3 and uses two data tracks in conjunction with all-sky imagery. This

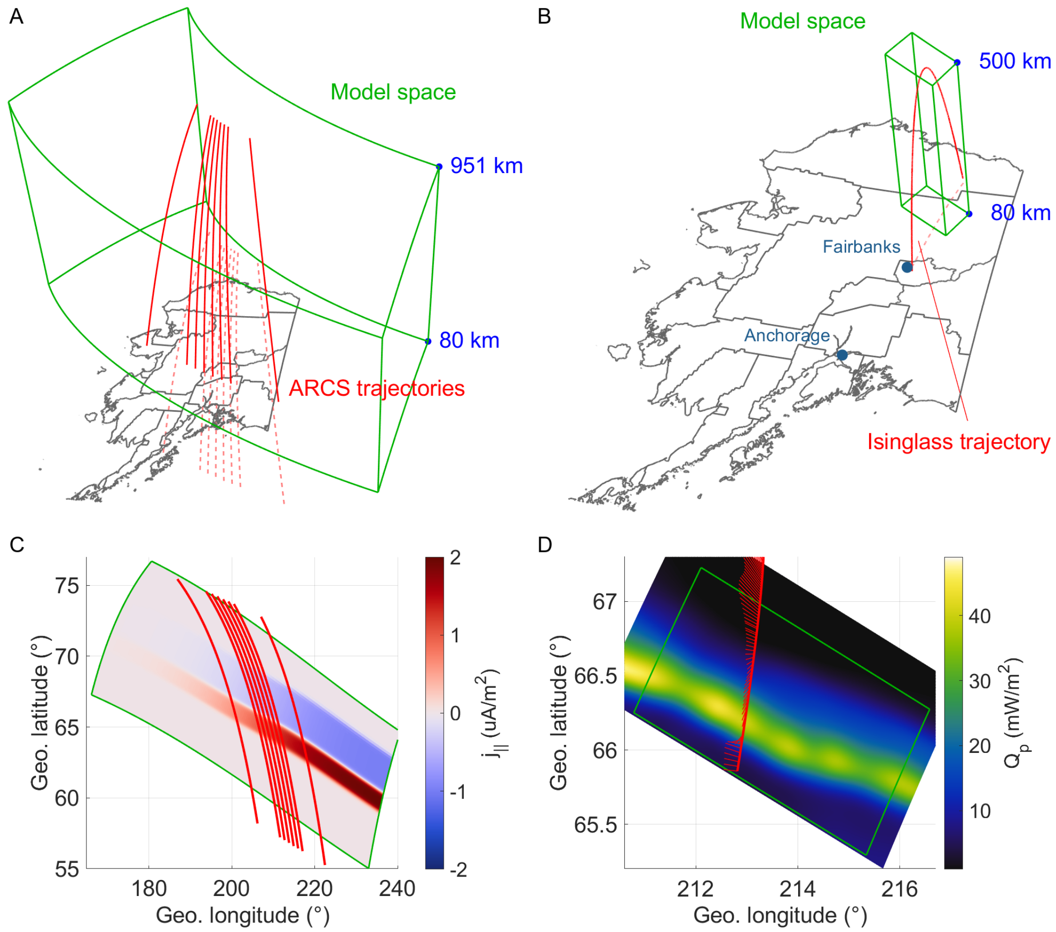

Figure 1. Geographical context relating to the simulations used in demonstrating the reconstruction and replication methods. **A**: The 3D simulation model space (green) and the ARCS trajectories (red), along with their ground tracks (red, dashed), in reference to Alaska. **B**: Same as panel A but with the Isinglass trajectory. **C**: Topside ionospheric FAC simulation driver (colormap) in reference to the model space (green) and ARCS orbits (red). **D**: Total precipitating energy flux (colormap) and plasma flow data (red) in reference to the model space (green outline). Data source: `https://rcweb.dartmouth.edu/lynchk`.

method repeats part of the replication methodology for each data track and then performs a weighted averaging on the interpolated flow maps (prior to enforcing electrostatics) with the weighting being based on the geometric distances to either data track.

In all three methods, one of the main difficulties in creating a continuous plasma flow map lies in the constraint that it is divergence-free, i.e. electrostatic (Ruohoniemi et al., 1989; Nicolls et al., 2014). Vector velocity fitting algorithms exist which handle this constraint. However, such algorithms will often create large flow vortices (diverging electric fields) which in our case act as spurious sources and sinks of FAC.

2.1 Reconstruction

This section provides a proof-of-concept reconstruction using an OSSE (Feb 1, 2015 at 10 UT, 23.2 MLT) from Lynch et al. (2024) wherein a localized "CubeSwarm" of virtual spacecraft generate synthetic data from the 3D auroral arc simulation as they orbit through (see Figure 1A). The simulation used in this section is data-inspired, but idealized; it is driven with a top-boundary map of a single pair of mostly east-west aligned FAC sheets with a slight bend in their profile and the amplitudes of which fade westward from ± 1 to 0 μA/m^2 over the span of the model space (see Figure 1C). The associated auroral arc precipitation input maps are of a similarly shaped arc embedded within the poleward FAC sheet peaking at an energy flux of 3 mW/m^2 and characteristic energy of 3 keV with gradient scale lengths of 40 km.

2.1.1 Reconstruction algorithm

With preconception of its general form, we construct the potential map out of a sum of a user-defined number, N_k, of east-north dependent pseudo-basis functions, ϕ_k, each governed by a set of parameters. The functional form for each of them is an inclined Gaussian ridge, i.e. a Gaussian profile northward that extrudes east- and westward with a constant sloped amplitude while following the curved boundary of the arc. This is done to find electric potential solutions that prioritize across-arc gradients while remaining relatively unstructured along the arc. The $\mathbf{E}\times\mathbf{B}$ plasma flow derived from this potential field is then compared against the virtual plasma flow data and the mean square difference is minimized over the parameter space.

The arc boundary is determined by applying a standard Sobel edge detection algorithm (Sobel, 2014) to the all-sky imagery derived Pedersen conductance. Given the idealistic nature of the OSSE used in demonstrating this method, this suffices, but we caution the reader regarding the complexities of determining less idealized arc boundaries. After determining an appropriate set of boundary points, they are least-squares fit against the following functional form:

$$b(x;\bar{A}) = \sum_{j=1}^{N_j} \left[A_{j1} + A_{j2} \tanh\left(\frac{x - A_{j3}}{A_{j4}} \right) \right], \tag{2}$$

with b the arc boundary, $\bar{A}$ the $N_j \times 4$ fitting boundary parameter matrix, N_j the user-defined number of summation terms, and x the linear magnetic east coordinate. Throughout this manuscript, the coordinates x, y, and z refer to linear magnetic east, north, and up in the northern hemisphere. The reason for the choice of summing hyperbolic tangents lies in the tendency of auroral arcs to be aligned magnetic east-west and to be relatively unstructured in this direction.

With this, we define our pseudo-basis potential ridge as

$$\phi_k(\mathbf{r};\bar{P},\bar{A}) = (P_{k1}x + P_{k2}) \exp\left[-\frac{\left(y - P_{k3} - b(x;\bar{A})\right)^2}{P_{k4}^2} \right], \tag{3}$$

where $\bar{P}$ is the $N_k \times 4$ potential parameter matrix, giving a total potential field of

$$\phi(\mathbf{r};\bar{P},\bar{A}) = \sum_{k=1}^{N_k} \phi_k(\mathbf{r};\bar{P},\bar{A}). \tag{4}$$

Parenthetically, prior work by (Clayton et al., 2021, Appx. A) aimed to instead warp the flow field via a coordinate transformation to along/across-arc coordinates, similar to those used by Marghitu (2012), but we have found the solution used here to be both simpler to implement and faster in this context.

The plasma flow data from the virtual spacecraft provide the flow vectors $\mathbf{v}_i = (v_{xi}, v_{yi})$ at positions $\mathbf{r}_i = (x_i, y_i)$ with i being the sample number. These flow data are Gaussian smoothed, which is done mindfully as this directly impacts the FAC sources in Eq. (1), but more on this in Section 4.2. With this, the electric field components, E'_x

and E'_y, to be compared against the plasma flow data are

$$\begin{aligned} E'_x(\mathbf{r}_i;\bar{P},\bar{A}) &= -\frac{\partial}{\partial x}\phi(\mathbf{r};\bar{P},\bar{A})\Big|_{\mathbf{r}_i} \\ &= -\sum_{k=1}^{N_k}\left[P_{k1}+\frac{2\gamma(\mathbf{r}_i;\bar{P},\bar{A})}{P_{k4}^2}(P_{k1}x_i+P_{k2})\frac{\partial b}{\partial x}\Big|_{x_i}\right]\exp\left[-\frac{\gamma(\mathbf{r}_i;\bar{P},\bar{A})^2}{P_{k4}^2}\right] \quad (5) \\ E'_y(\mathbf{r}_i;\bar{P},\bar{A}) &= -\frac{\partial}{\partial y}\phi(\mathbf{r};\bar{P},\bar{A})\Big|_{\mathbf{r}_i} \\ &= \sum_{k=1}^{N_k}\frac{2\gamma(\mathbf{r}_i;\bar{P},\bar{A})}{P_{k4}^2}(P_{k1}x_i+P_{k2})\exp\left[-\frac{\gamma(\mathbf{r}_i;\bar{P},\bar{A})^2}{P_{k4}^2}\right], \quad (6) \end{aligned}$$

with $\gamma(\mathbf{r};\bar{P},\bar{A}) = y - P_{k3} - b(x;\bar{A})$ and

$$\frac{\partial b}{\partial x} = \sum_{j=1}^{N_j}\frac{A_{j2}}{A_{j4}}\operatorname{sech}^2\left(\frac{x-A_{j3}}{A_{j4}}\right). \quad (7)$$

From here, with $\mathbf{B} = -B\hat{z}$, we rotate the electric field providing (non-optimized) plasma flow:

$$\mathbf{v}'(\mathbf{r};\bar{P},\bar{A}) = v'_x\hat{x} + v'_y\hat{y} = \frac{\mathbf{E}'\times\mathbf{B}}{B^2} = \frac{1}{B}\big(-E'_y\hat{x} + E'_x\hat{y}\big). \quad (8)$$

This reduces the problem to finding the parameter matrix, $\bar{P}^0$, which solves

$$\min_{\bar{P}}\sum_i \left\|\big(v'_x(\mathbf{r}_i;\bar{P},\bar{A}^0), v'_y(\mathbf{r}_i;\bar{P},\bar{A}^0)\big) - (v_{xi}, v_{yi})\right\|^2, \quad (9)$$

where $\bar{A}^0$ is the best fitting boundary parameter matrix, such that the continuous plasma flow map, v_c, is given by

$$\mathbf{v}_c(\mathbf{r}) = \mathbf{v}'(\mathbf{r};\bar{P}^0,\bar{A}^0), \quad (10)$$

and subsequently the continuous potential map used to drive ionospheric models is

$$\phi_c(\mathbf{r}) = \phi(\mathbf{r};\bar{P}^0,\bar{A}^0). \quad (11)$$

By using the potential ridges, we prioritize solutions for ϕ_c that have sheet-like morphology in contrast to what has been done before (Kamide et al., 1981; Amm, 1997; Nicolls et al., 2014; Bristow et al., 2016; Laundal et al., 2022). This maintains strong potential gradients normal to the arc boundary, as may be expected from basic current continuity considerations and observations of electric field variability near arcs (Marghitu, 2012).

2.1.2 Reconstruction example

Figure 2 shows an example use of the reconstruction algorithm. This example was developed for the proposed ARCS mission (Lynch et al., 2024) to verify the ability of plasma flow reconstruction given a local grouping of spacecraft. The virtual orbits are

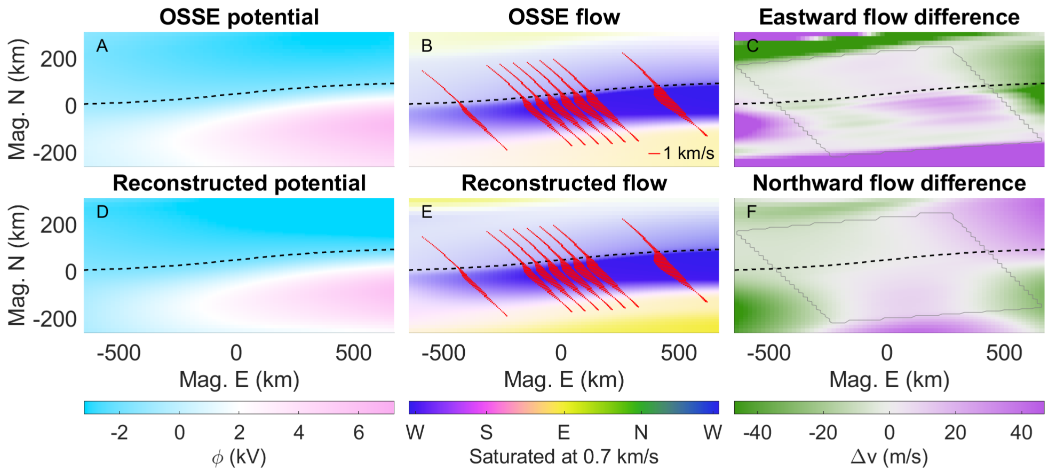

Figure 2. Example of a plasma flow field reconstruction. **A**: The electric potential map used to drive the OSSE with the boundary, b, overlaid. **B**: The resulting flow field with the virtual flow data points, $\mathbf{v}_i$, (red) interpolated from it. The color representation of flow has the direction depicted by hue and the intensity by the color saturation. **D**, **E**: The reconstructed electric potential, ϕ_c, and flow, $\mathbf{v}_c$. **C**, **F**: The difference between the reconstructed and OSSE east- and northward flow with the gray outline being the region of interest. Data source: `https://rcweb.dartmouth.edu/lynchk`.

arranged densely to provide maps of along- and across-arc gradients. The black dashed lines are the imagery derived boundary, b. The plasma flow vectors, $\mathbf{v}_i$, are overlaid in red. The reconstructed electric potential, ϕ_c, and reconstructed flow, $\mathbf{v}_c$, match well within the spacecraft region (gray outline in Fig. 2C, F) as per design. The maximum absolute flow difference in this region is 47 m/s eastward and 28 m/s northward with averages of 5(12) and 5(8) m/s.

2.1.3 Possible improvements

A different choice of the potential ridges, ϕ_k, can be used to stretch the well-fitted region as presently the goodness-of-fit rapidly decreases when moving away from the spacecraft. The electric field resulting from a single ridge i.e. Eqs. (5-6), far from the fitting region is

$$\lim_{\mathbf{r}\to\infty} E_{xk}(\mathbf{r};\bar{P},\bar{A}) = -P_{k1}\exp\left[-\frac{(y-P_{k3}-b_{\pm\infty})^2}{P_{k4}^2}\right] \tag{12}$$

$$\lim_{\mathbf{r}\to\infty} E_{yk}(\mathbf{r};\bar{P},\bar{A}) = \frac{2}{P_{k4}^2}(P_{k1}x+P_{k2})(y-P_{k3}-b_{\pm\infty})\exp\left[-\frac{(y-P_{k3}-b_{\pm\infty})^2}{P_{k4}^2}\right], \tag{13}$$

where $b_{\pm\infty} = \sum_j (A_{j1} \pm A_{j2})$ and $\partial b/\partial x(x \to \pm\infty) \to 0$. Here, E_{xk} remains finite, but E_{yk} diverges as $|y| < \infty \wedge x \to \infty$. As models often require extended coverage surrounding the region of interest into which the flow map needs to extrapolate, slowing down this divergence would provide improved solutions for outside the spacecraft region. Lastly, incorporating weighted fitting would provide error estimates for reconstructions from real data as opposed to an OSSE, e.g. weights of $w_i = 1/\sigma_i^2$ with σ_i being instrument error.

2.2 Replication

The second method of developing continuous topside ionospheric plasma flow maps uses individual, approximately across-arc data tracks of plasma flow data in conjunction with all-sky, multi-spectral imagery. In this method, data points are replicated in the along-arc direction using direct and indirect information from the imagery. Primary *and* secondary boundaries are determined along which the data track is translated, scaled, and the flow data are rotated to be tangent with the primary boundary. The example here uses dataset "c5" from Clayton et al. (2021) on March 2, 2017 at 7:54:10 UT (20.2 MLT).

2.2.1 Arc boundary definitions

Determining the arc boundaries from multi-spectral imagery data first requires an inversion (Grubbs II, Michell, Samara, Hampton, Hecht, et al., 2018; Grubbs II, Michell, Samara, Hampton, & Jahn, 2018) to a map of total energy flux, Q_p, and characteristic energy, E_p, of the precipitating electrons. From these a proxy for the Pedersen conductance is made which is done using Eq. (3) by Robinson et al. (1987):

$$\Sigma_P(x, y) = \frac{40E_p(x, y)}{16 + E_p^2(x, y)} Q_p^{1/2}(x, y), \tag{14}$$

with E_p in keV and Q_p in mW/m^2. It is, of course, possible to use multi- and/or two-stream transport models (similar to how Q_p and E_p are determined), such as the GLobal airglOW (GLOW) model (Solomon, 2017), or look-up tables generated by such models, to determine a more accurate Pedersen conductance; however, Eq. (14) suffices in providing a proof-of-concept.

With this, the primary and secondary arc boundaries are established in one of two ways: 1) finding the magnetic latitude of the first two most prominent edges at each mag-

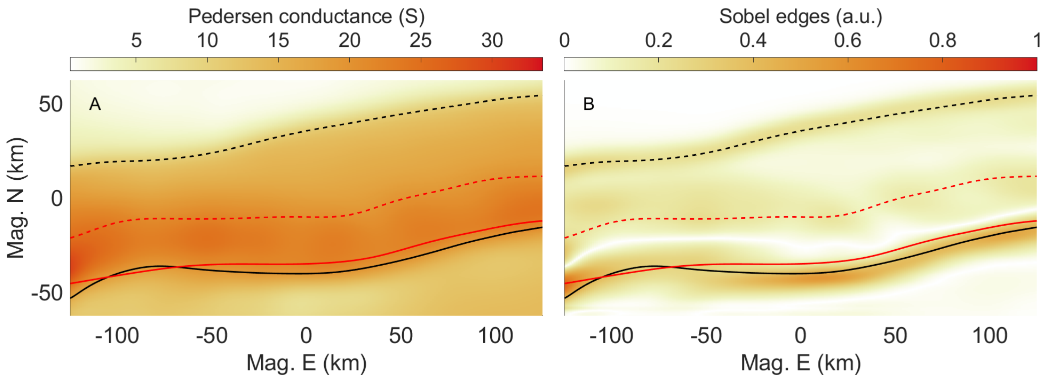

Figure 3. Primary (solid) and secondary (dashed) boundaries using Pedersen conductance and contour lines at 19.1 S and 10.5 S (black). In red are the boundaries determined using the energy flux (not shown) with the steepest gradient method, as is done by Clayton et al. (2019, 2021). **A**: Pedersen conductance determined via Eq. (14). **B**: Magnetic northward Sobel convolution of the Pedersen conductance. Both sets of boundaries have an approximate smoothing window of 15 km.

netic longitude using Sobel edge detection (Sobel, 2014) in the magnetic northward direction, or 2) following a contour line at two isovalues which can be chosen directly, or determined at the locations of the central two most prominent edges along the data track. In either case, the boundary is Gaussian smoothed. Both of these methods can be applied to the *either* the total energy flux *or* Pedersen conductance. Clayton et al. (2019, 2021) use method 1 on the total energy flux, whereas, for the remainder of this paper, we use boundaries determined using Pedersen conductance contour lines. Figure 3 shows the Pedersen conductance and its magnetic northward Sobel convolution along with the primary and secondary boundaries determined using method 2 with Pedersen conductance and method 1 with total energy flux.

2.2.2 *Flow data replication*

After the boundaries are determined, they are used to replicate the plasma flow data track, but first, the flow data are Gaussian smoothed (more on this in Section 4.2) and, prior to doing any replication, we split the plasma flow into two components: 1) the background flow, $\mathbf{v}_{\rm bg}$, treated as a constant, large-scale disturbance, and 2) the small-scale disturbances imposed by the arc, $\mathbf{v}_{\text{arc}}$:

$$\mathbf{v}(\mathbf{r}) = \mathbf{v}_{\text{arc}}(\mathbf{r}) + \mathbf{v}_{\text{bg}}. \tag{15}$$

Throughout the remainder of Section 2, this background flow is put aside and is only added back when performing 3D simulations (see Section 3.2). In absence of background flow, the most basic model of an auroral arc is composed of only across-arc flow shear (Marghitu, 2012). Thus, we define the background flow such that, once removed, the arc flow at the intersection of the data track and the primary boundary is tangent to that boundary. Furthermore, this simplistic model has the arc defined as a band of enhanced conductance in which we expect the electric field to decrease (Marghitu, 2012; Kelley, 2009). Thus, we replicate these data along the arc boundaries, while remaining tangent to it, and scaling such that the shorted out electric fields remain inside the area of enhanced conductance. This leads to the following plasma flow data track replication algorithm:

1. The original data track is translated in the east-north plane by some amount following the primary arc boundary such that the original and replicated flow data are equal at the primary boundary-track intersections.
2. The replicated data track is scaled in the along-track direction such that the original and replicated flow data are equal at the secondary boundary-track intersections.
3. The flow data of the replicated track is rotated by a constant angle per data track such that it remains to be tangent to the primary arc boundary.
4. This replication is repeated for multiple translations along the arc until the top-boundary is filled with a sufficient replication rate.

Figure 4 illustrates these steps given the boundaries of Figure 3. The left panel of Figure 4 shows two examples of how replications of the original trajectory are translated and scaled. The western replication example is scaled down to have the data at the red cross meet the secondary boundary, while the eastern replication is scaled up to do the same. The right panel shows the replication, but done only for a few instances for illustration purposes. This also shows the rotated flow vectors keeping tangent with the primary boundary.

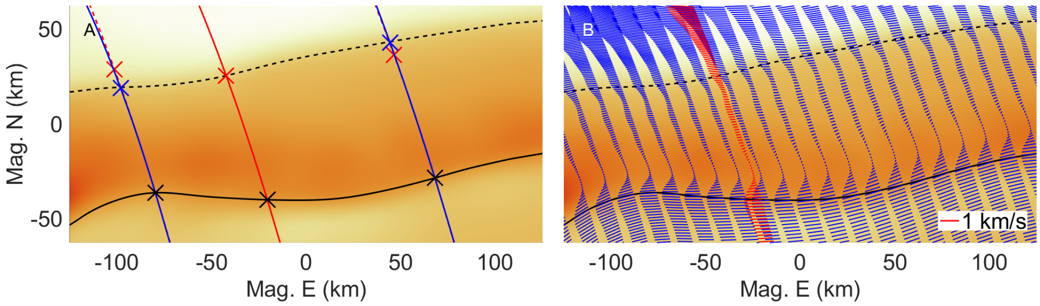

Figure 4. In situ trajectory flow data replication overlaid on the same conductance map from Figure 3A. **A**: Two example replications (blue) of the original trajectory (red) along the primary arc boundary (solid black). The black crosses have the same flow data. The red/blue crosses indicate flow data before/after scaling to meet up with the secondary arc boundary (dashed black). **B**: A low density replication (blue) along with the original, smoothed flow data (red). Data source: `https://rcweb.dartmouth.edu/lynchk`.

2.2.3 Enforcing electrostatic flow

The replication procedure does not, generally, produce a flow field that is divergence-free, implying a non-electrostatic component to the electric field which we seek to remove for use in electrostatic models. The replicated flow data are interpolated onto the model grid (more on this in Section 4.2). This section outlines two choices of fitting an electric potential map to this interpolated flow field, $\mathbf{v}_{\mathrm{arc}} = \mathbf{E}_{\mathrm{arc}} \times \mathbf{B}/B^2$, where $\mathbf{B}$ is the magnetic field from Eq. (8) and $\mathbf{E}_{\mathrm{arc}}$ is the arc disturbed ionospheric electric field perpendicular to $\mathbf{B}$. The Helmholtz decomposition of the interpolated flow fields' associated electric field reads:

$$\mathbf{E}_{\mathrm{arc}}(\mathbf{r}) = \mathbf{E}_I(\mathbf{r}) + \mathbf{E}_S(\mathbf{r}) = -\nabla\phi_c(\mathbf{r}) + \nabla \times \mathbf{A}(\mathbf{r}), \qquad (16)$$

where ϕ_c is the electric potential map we are looking for and $\mathbf{A}$ is the vector potential. We want to remove the non-electrostatic part, i.e. find the irrotational electric field, $\mathbf{E}_I$, and remove the solenoidal field, $\mathbf{E}_S$, in a way that best agrees with the interpolated flow field. Two choices of doing so are:

1. **Brute force**: Perform a least-squares fitting algorithm (Levenberg–Marquardt in our case) that fits a potential map, ϕ, to minimizes the residual between the

original and irrotational fields:

$$\min_{\phi} \|\nabla \times \mathbf{A}(\mathbf{r})\|^2 = \min_{\phi} \|\nabla\phi(\mathbf{r}) + \mathbf{E}_{\mathrm{arc}}(\mathbf{r})\|^2 = \min_{\phi} \sum_{i,j} \left\| (\nabla\phi)_{ij} + \mathbf{E}_{\mathrm{arc},ij} \right\|^2, \quad (17)$$

the solution of which, ϕ_c, is the continuous potential map we want.

2. **Fourier Representation Of Poisson's Equation (FROPE)**: We take the divergence of Eq. (16) to get Poisson's equation:

$$\nabla^2\phi_c(\mathbf{r}) = -\nabla \cdot \mathbf{E}_{\mathrm{arc}}(\mathbf{r}). \quad (18)$$

We can solve for the particular solution using a Fourier representation:

$$-\|\mathbf{k}\|^2\tilde{\phi}_c(\mathbf{k}) = -i\mathbf{k} \cdot \tilde{\mathbf{E}}_{\mathrm{arc}}(\mathbf{k}) \implies \tilde{\phi}_c(\mathbf{k}) = i\frac{\mathbf{k} \cdot \tilde{\mathbf{E}}_{\mathrm{arc}}(\mathbf{k})}{\|\mathbf{k}\|^2}, \quad (19)$$

where $\mathbf{k} = (k_x, k_y)$ is the wave vector, such that the particular potential solution map is

$$\phi_p(\mathbf{r}) = (\mathcal{F}^{-1}\tilde{\phi}_c)(\mathbf{r}). \quad (20)$$

The homogeneous solution, ϕ_h, where $\phi_c = \phi_p + \phi_h$ and $\nabla^2\phi_h = 0$, usually is determined using a Laplace solver enforcing the boundary conditions of $\mathbf{E}_{\mathrm{arc}}$. However, in order to have more control of the weighting of the plasma flow generated by our replication and interpolation procedure, we opt for one of two options: the first, $\phi_h = \phi_a$, has the average electric field before and after enforcing electrostatics remain, i.e.

$$\phi_a(\mathbf{r}) = \langle -\nabla\phi_p(\mathbf{r}) - \mathbf{E}_{\mathrm{arc}}(\mathbf{r})\rangle \cdot \mathbf{r}. \quad (21)$$

This option requires no optimization (i.e. it can be computed directly from the particular solution found above), whereas a second option, $\phi_h = \phi_b^m$, solves the optimization problem

$$\min_{\bar{F}} \left\| -\nabla\big(\phi_p(\mathbf{r}) + \phi_b^m(\mathbf{r}; \bar{F})\big) - \mathbf{E}_{\mathrm{arc}}(\mathbf{r}) \right\|^2 \;\text{ with }\; \mathbf{r} \in \mathcal{M}, \quad (22)$$

where $\bar{F}$ is an $m{\times}2$ parameter matrix, $\mathcal{M}$ is a user defined masking domain surrounding the primary and/or secondary boundary, and original data track, and ϕ_b^m is the most general polynomial of degree m in x and y that satisfies Laplace's equation:

$$\phi_b^m(\mathbf{r}; \bar{F}, \rho) = \sum_{n=1}^{m} \sum_{q=0}^{\lfloor n/2 \rfloor} (-1)^q \left[\frac{F_{n1}}{\rho^{n-1}} \binom{n}{2q+1} x^{2q+1} y^{n-2q-1} + \frac{F_{n2}}{\rho^{n-1}} \binom{n}{2q} x^{2q} y^{n-2q} \right], \quad (23)$$

where ρ is a scaling parameter used to facilitate fitting higher order terms. An example for $m = 2$ and $\rho = 10$ m gives

$$\phi_b^2(\mathbf{r}, \bar{F}) = F_{11}x + F_{12}y + \frac{F_{21}}{10}\left(x^2 - y^2\right) + \frac{F_{22}}{10}xy. \tag{24}$$

Note that x, y, and ρ in meters and $\bar{F}$ in V/m has ϕ_b^m in volts. When solving for this optimization problem the initial guess is taken to be ϕ_a.

To show this is the most general case, take the complex polynomial of degree m

$$p(z) = \sum_{n=0}^{m} F_n z^n, \text{ where } z^n = (x + iy)^n = \sum_{q'=0}^{n} \binom{n}{q'} x^{q'} (iy)^{n-q'}, \tag{25}$$

and recognize that the homogeneous polynomial z^n is analytic which therefore has harmonic real and imaginary parts (Ahlfors, 1953). This gives two parameters, the real and imaginary parts of F_n, for each value of n. To show uniqueness, we recognize that the Laplacian maps homogeneous polynomials of degree n to those of degree $n-2$, the domain and image of which have dimensions n and $n-2$ respectively. By the rank-nullity theorem, this means the dimension of the kernel of the Laplacian is $n - (n - 2) = 2$, so we have found all solutions.

Along with the interpolated flow field (column 1), examples of the brute force and FROPE are shown in Figure 5 (columns 2-3). The divergence panel shows that of the interpolated flow field and indicates the location of rotational signatures which are interpretable as Alfvénic. Although the brute force method is easiest to justify being the "best" fit, it is also by far the slowest. The FROPE method, on the other hand, has the advantage of using the fast Fourier transform method and it compares reasonably well, even when using the direct harmonic solution, ϕ_a. This is illustrated in Figure 6 which shows the residual between the brute force solution and the potential from Eq. (20) compared against a masked and unmasked harmonic fit. A constant background electric field match, i.e. a harmonic function that is constant sloped plane, ϕ_a, is a first order solution in this particular case but this requires further confirmation for other cases. The masking acts as a binary placeholder for a continuous error based weighting map. Such an improved map will aid in constraining the potential in the corners of the model space (see Figure 6C).

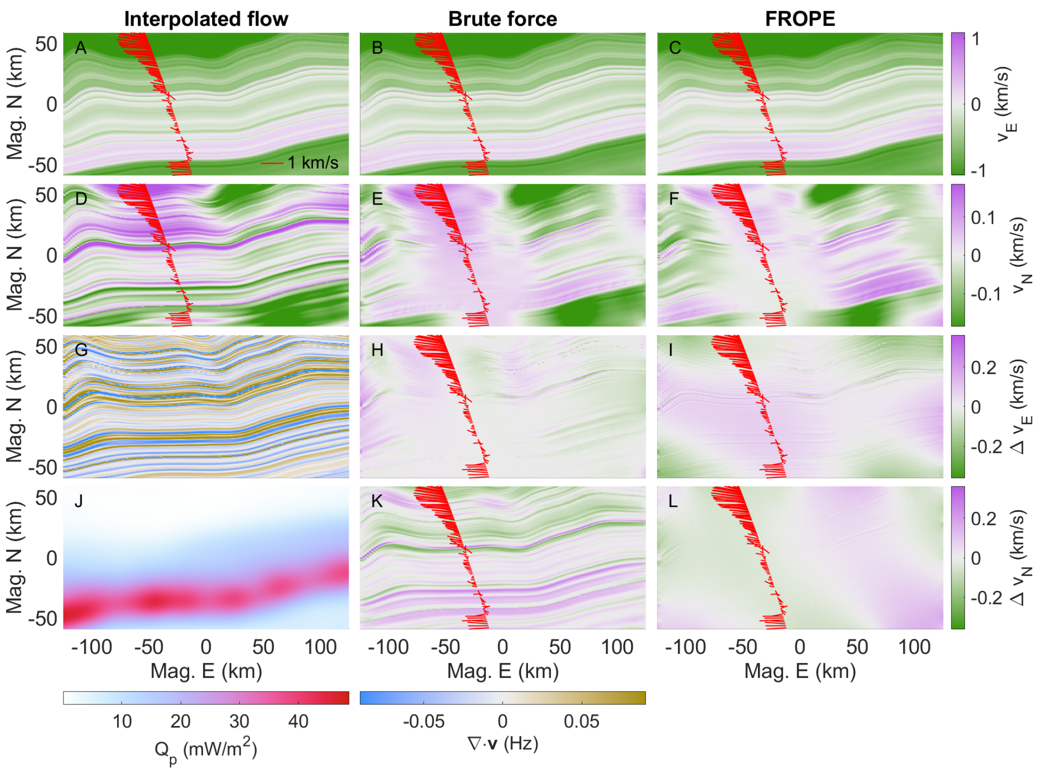

Figure 5. Comparison of methods for determining a potential map from an interpolated flow map, $\mathbf{v}_{\mathrm{arc}}$. In red are the in situ plasma flow data which have no smoothing applied in an effort to stress test these methods. **A-C**: Eastward plasma flow from interpolation, the brute force method, and the FROPE method. **D-F**: Same as panels A-C but northward. **G**: Divergence of the interpolated flow. **H**, **K**: Difference in east- and northward flow between brute force and interpolated. **I**, **L**: Difference in east- and northward flow between the FROPE and brute force. **J**: Total precipitating energy flux (for reference). Data source: `https://rcweb.dartmouth.edu/lynchk`.

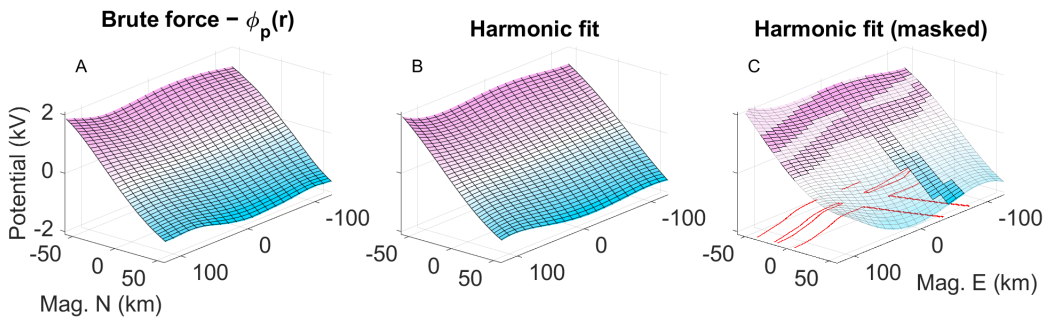

Figure 6. Validity of a harmonic function fit. **A**: Residual potential between brute force fitting and Eq. (20). **B**: Unmasked harmonic function fit from Eq. (23) with $m = 5$ and $\rho = 10$ m. **C**: Same as panel B but masked with the mask, $\mathcal{M}$, in red.

2.2.4 Replication example

Figure 7 shows the replication methodology applied to the "c5" example by Clayton et al. (2021) (see their Table 1). The top row has the scaling and rotating applied, whereas the bottom row has neither applied. For the top row, the masked 2-sigma ranges of the residuals in enforcing electrostatics are ± 106 m/s eastward and $\pm^{142}_{140}$ m/s northward. For the bottom row, these numbers are ± 84 m/s and ± 101 m/s. Qualitatively, the applied scaling to the replication results in a co-location of the shorted-out electric field and the auroral precipitation as seen by the Σ_P contour lines in panel A, in comparison to panel D. Secondly, the applied rotation provides more streamlined plasma flow, in the literal sense, as seen by the change from southwest to west to southwest flow in panel A. In contrast, without rotation the flow remains westward resulting in a changing angle between the electric field and the conductance gradients. This has physical effects on auroral current closure (see Eq. (1)).

2.3 Weighted replications

In the event of a conjunction between auroral imagery and two flow data tracks, the replication method can be repeated for both tracks up to and including the interpolation step (at the beginning of Section 2.2.3). Both replications use the same primary and secondary boundaries as well as the same background flow, $\mathbf{v}_{\mathrm{bg}}$. This background flow is determined by whichever replication is done first. The flow data smoothing is also performed with approximately equal Gaussian filter physical window widths.

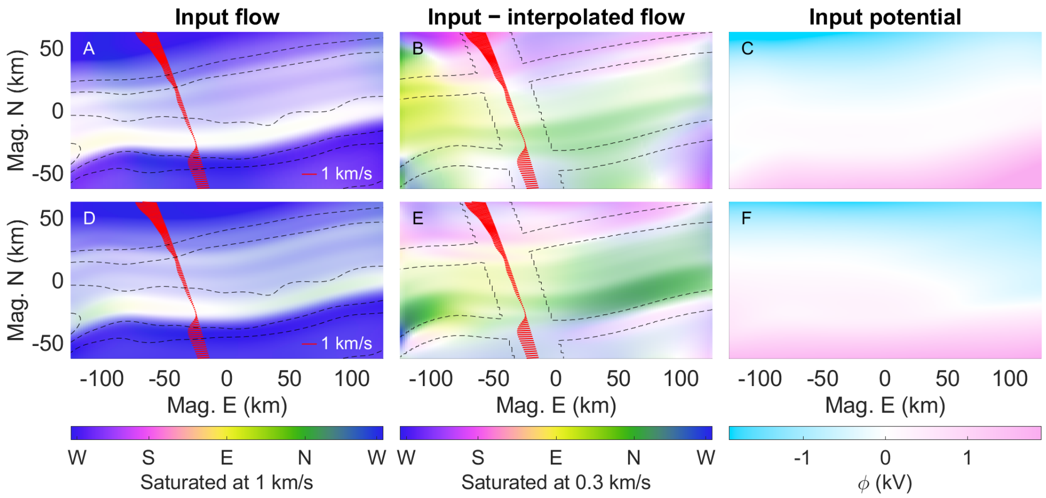

Figure 7. Input flow and potential maps used to drive simulations with (top row) and without (bottom row) replication scaling/rotating. **A**, **D**: Hue-saturation plots of input flow maps, $-\nabla\phi_c$, with contour lines of Pedersen conductance, Σ_P. **B**, **E**: Difference between input and interpolated plasma flow maps, i.e. $-\nabla\phi_c - \mathbf{v}_{\text{arc}}$, with masking contours where the harmonic function is fit. **C**, **F**: Input potential maps, ϕ_c. Data source: `https://rcweb.dartmouth.edu/lynchk`.

Once both data tracks have their replication and subsequent interpolated flow fields, they are weighted averaged with the weighting functions

$$w_A(\mathbf{r}) = \frac{1}{2}\left[1 + \tanh\left(\frac{d_{\min,B}(\mathbf{r}) - d_{\min,A}(\mathbf{r})}{s_w}\right)\right], w_B(\mathbf{r}) = 1 - w_A(\mathbf{r}). \tag{26}$$

Here, $d_{\min,A}$ is a map of the shortest straight-line distances from points $\mathbf{r}$ to data track A and similarly for data track B. This configuration of weighting allows for two intersecting data tracks. The scale length, s_w, will introduce flow gradients and has to be chosen with care. From here we have a new interpolated arc-disturbed plasma flow,

$$\mathbf{v}_{\text{arc}}(\mathbf{r}) = w_A(\mathbf{r})\mathbf{v}_{\text{arc},A}(\mathbf{r}) + w_B(\mathbf{r})\mathbf{v}_{\text{arc},B}(\mathbf{r}), \tag{27}$$

from which the methodology from Section 2.2.3 takes over. This ensures electrostatics, but it should be mentioned that, on top of the divergences still remaining in either data track's interpolated field, this weighting function introduces additional divergence of the form

$$(\nabla \cdot \mathbf{v}_{\text{arc}})_w = \nabla w_A(\mathbf{r}) \cdot (\mathbf{v}_{\text{arc},A} - \mathbf{v}_{\text{arc},B}). \tag{28}$$

This weighting function, however, has small northward gradients and the interpolated flows are expected to not vary much eastward, i.e. ∇w_A is approximately orthogonal to

$\mathbf{v}_{\mathrm{arc},A} - \mathbf{v}_{\mathrm{arc},B}$ resulting in minimal diverging flow. This ensures that the subsequent Helmholtz decomposition provides an electrostatic solution of the final flow map that does not stray far from the interpolated flow map.

2.3.1 Weighted replication example

To illustrate the double replication methodology, a conjunction from the *Swarm-over-Poker-2023* campaign is used (Feb - March 2023, Poker Flat Research Range, AK). This campaign facilitated conjunctions of (among a variety of other data) ion flow data from the Thermal Ion Imagers (TII) (Knudsen et al., 2017) on ESA's Swarm mission, convection flow data from AMISR's Poker Flat Incoherent Scatter Radar (PFISR) (Kelly & Heinselman, 2009; Nicolls & Heinselman, 2007; Heinselman & Nicolls, 2008), and multi-spectral, all-sky imagery from the Poker Flat DASC (Conde et al., 2001). This season provides a rich source of heterogeneous auroral observations for the winter months of 2023. Our example uses data from March 19 at 8:23:44 UT (20.4 MLT).

To circumvent the flagged poor-quality data of the Swarm ram ion flow component for this conjunction, the data streams from both the vertical and horizontal TII instruments are simultaneously fit using locally weighted scatterplot smoothing to average the two streams while suppressing outliers from the overall trend.

Figure 8A summarizes this event showing an auroral arc peaking at $Q_p \approx 30$ mW/m^2 (and $E_p \approx 7$ keV, not shown) with some along-arc structure. The left trajectory shows ion flow data from Swarm B and the right data track shows convection flow data from PFISR. Panel B also shows the Pedersen conductance (this time inverted using GLOW (Solomon, 2017)) which is used to determine the arc boundaries, and panel C shows the weighting function used for the Swarm data. The bottom row gives the final continuous plasma flow maps when using only the Swarm data, or the PFISR data, or both. The individual reconstructions in panels D and E are dissimilar which is to be expected given the along-arc structure; the flow data are different at the two locations surrounding the arc, as are the conductance gradients. The final combined flow (panel F) before and after enforcing electrostatics have residual 2-sigma standard range of ± 91 m/s eastward and $\pm^{157}_{159}$ m/s northward.

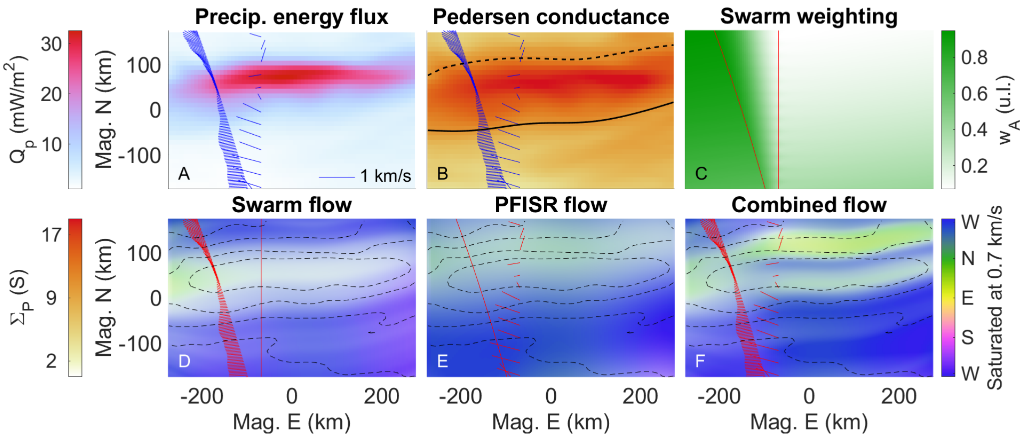

Figure 8. Weighted replication example. **A**: Precipitating total electron energy flux with plasma flow data from Swarm (left trajectory) and PFISR (right data track) in blue. **B**: The GLOW derived Pedersen conductance with the primary (solid) and secondary (dashed) boundaries overlaid. **C**: The weighting map, w_A, used for the Swarm data with a scale length of $s_w = 200$ km. **D**-**F**: Resulting flow maps from using only Swarm data, only PFISR data, and from using both datasets, respectively. The dashed contours are of Pedersen conductance. Data sources: `http://optics.gi.alaska.edu/optics` (DASC), `https://data.amisr.com/database` (PFISR), and `https://swarm-diss.eo.esa.int` (Swarm).

3 Auroral Ionosphere 3D Modeling with Potential Map Estimates

3.1 The GEMINI model

To investigate the effects of continuous topside ionospheric plasma flow maps in conjunction with auroral precipitation, we use state-of-the-art 3D ionospheric simulations provided by the Geospace Environment Model of Ion-Neutral Interactions (GEMINI) (M. D. Zettergren & Semeter, 2012; M. Zettergren & Snively, 2019). This is a multi-fluid (6 ions + electrons), quasi-electrostatic model with its calculations of particle continuity consisting of chemical production/loss and photo/impact ionization. Calculations of local densities, plasma flows, and temperatures are treated self-consistently and the model includes thermal conduction heat flux, collisional heating, thermoelectric electron heat flux, and inelastic cooling/heating from photoelectrons. This is supplemented with Maxwell's equations and, at the time of writing, includes no displacement current or magnetic induction effects. With this, the system is solved through enforcing divergence-free currents, curl-free electric fields, and invoking Ohm's law. A full description of governing equations solved by GEMINI is given in M. D. Zettergren and Snively (2015, Appx. A).

3.2 Simulation examples

Figure 9 shows GEMINI output data with Figure 7C as the plasma flow driver and the same precipitation data used by example "c5" from Clayton et al. (2021). Unlike previous figures, here the figure/simulation has $\mathbf{v}_{\text{bg}}$ put back in. This simulation has $440\times 504\times 814$ nonuniform cells in the magnetic east, north, and up directions and runs for 90 seconds. The calculated FAC slice is taken at an altitude of 200 km, but is plotted at 80 km for visualization purposes. Similarly, the electron density slice is taken at the center but plotted at the eastern wall. In order to visualize FAC closure, we opt for current flux tubes which are made possible by the GEMINI enforced condition of $\nabla\cdot\mathbf{j} = 0$ and the use of streamlines sourced at closed elliptical curves (solid black curves). This enables an astute interpretation of auroral current closure by showing where a patch of FAC joins back with the magnetosphere, or where a region of Hall current exits the model space. The dotted black and blue curves show the projection of the terminating ends of the flux tubes onto the FAC map. The green flux tube (27.8 kA) represents a traditional example of FAC closure via the Pedersen layer, closing down between 118 - 159 km. The

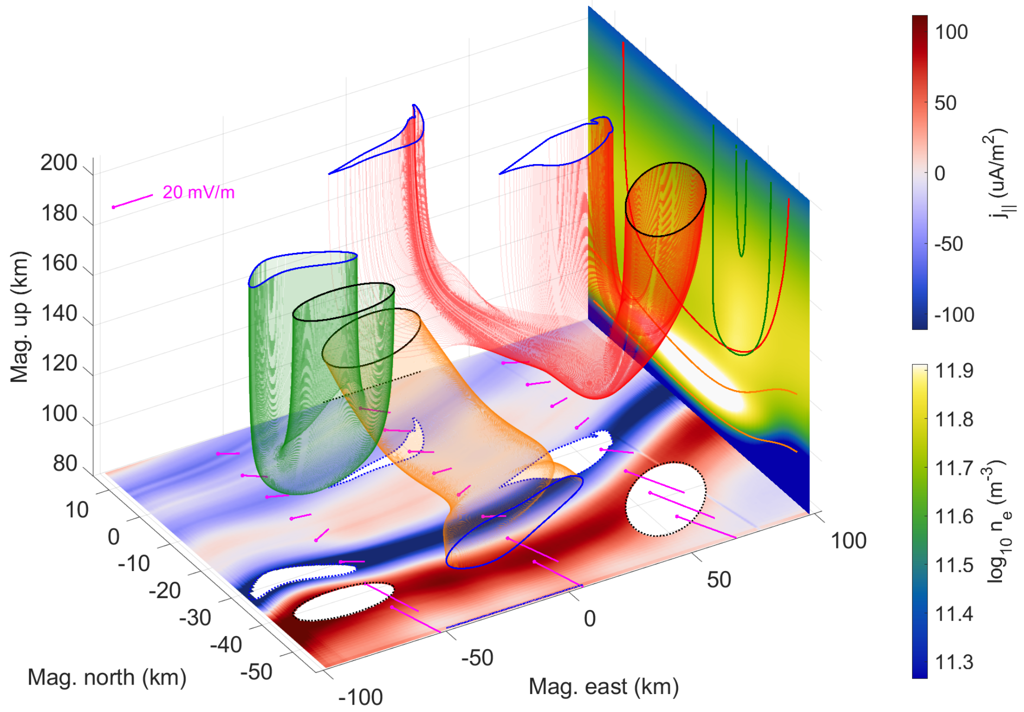

Figure 9. Plasma flow driven GEMINI output with input from the potential in Figure 7C. Current flux tubes are colored for distinction purposes and start/end at solid black/blue curves. The orange flux tube runs in reverse from the poleward to the equatorward boundary walls. **East side**: A north-up slice of electron density taken at 0 km east along with flux tube outline projections. **Bottom side**: An east-north slice of FAC (with parallel being down) taken at 200 km altitude along with flux tube start/end curve projections (dashed) and electric field vectors (magenta). These electric field vectors include the background electric field.

orange tube (31.0 kA) runs underneath it near the Hall layer and shows exchange between a region of Hall current and Pedersen current (see magenta electric field vectors) up near the bottom of the Pedersen layer. This tube enters at the poleward wall between 90 - 110 km in altitude, spans between 87 - 100 km at its lowest point, and exits the equatorward wall between 101 - 126 km. The red flux tube (23.9 kA) is, to some extent, a combination of these two, and has two exit regions. When this tube runs out of upward FAC to close through in its adjacent current sheet, it continuous onto the next upward FAC sheet poleward of it where the remaining 2.5 kA is closed.

To show the effects of steps 2 and 3 of section 2.2.2 we run additional simulations (at a lower resolution of $128 \times 512 \times 212$) using the same precipitation maps but with

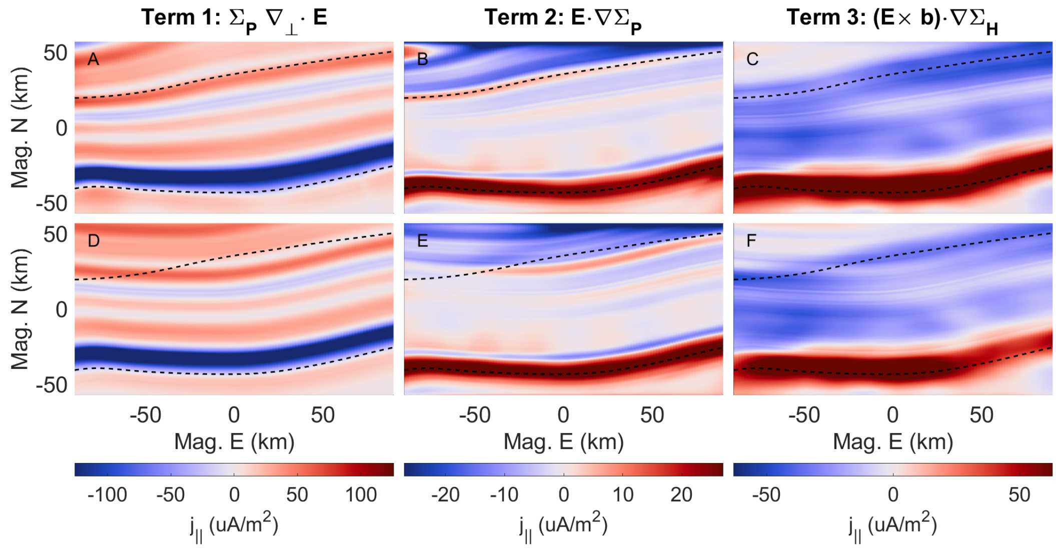

Figure 10. Calculated FAC components from Eq. (1). **A**-**C**: Terms 1 through 3 respectively split from the FAC map shown in Figure 9 along with arc boundaries (dashed). **D**-**F**: Same as terms from the top row but with replication scaling and rotating turned off.

the replication scaling and rotating turned on and off (see Figure 7D-F). Figure 10 divides the topside ionospheric FAC maps of both simulations into the three terms from Eq. (1) in order to look at the effects of the plasma flow shear and precipitation gradients separately. Figure 10D shows sensible results given a single arc boundary, but panels E and F illustrate an amalgamation of two apparent arc profiles at the poleward edge of the arc; even though this replication is fully transparent to the secondary boundary, the Pedersen and Hall conductance gradients cause the secondary boundary to substantiate. In contrast, Figures 10A-C show clean alignment between both arc boundaries for all three FAC terms.

4 Discussions

4.1 Improvements to auroral plasma flow mapping

Figure 9 indicates that even for basic examples of auroral arc systems, the morphology of current closure is 3D in nature. The green flux tube depicts a more instinctive auroral current closure type (Mallinckrodt, 1985) using largely Pedersen currents to close, however, the red flux tube illustrates a less common view of FAC current closure; not all current from one FAC sheet has to close with its neighbouring sheet. The section of the sourced FAC furthest equatorward has to "dig" deeper into the Hall layer, subsequently horizontally rotating, in search of another closure path. Secondly, the orange flux tube is mostly Hall current, but includes divergence, i.e. the last term in Eq. (1), which is being fed by Pedersen currents as the tube descends from regions of higher conductivity (see the electron density panel). The Pedersen current being used by this closure can no longer be used to close FACs, which is how diverging Hall currents can indirectly effect topside ionospheric currents. Moreover, FAC closure is not restricted to the 90 - 130 km altitude range where Pedersen and Hall conductivities maximize; depending on the perpendicular distance from the FAC sheet inflection line, Pedersen closure can happen at altitudes as high as 159 km in this instance. From a current flux conservation standpoint, this is a matter of balancing the lower conductivity at these heights with a larger flux tube cross-section.

All this 3D structure is attributable to the interplay of the altitude dependent Pedersen and Hall conductivities as a region of current follows the path of least resistance. To better understand electrostatic auroral arc scale science, and the non-passive role the ionosphere plays in quasi-static MI coupling, these 3D features require further studies, which in turn requires 3D auroral simulations and thus this provides the need for continuous, topside ionospheric, electrostatic plasma convection maps.

We have developed techniques for creating such maps from sparse, heterogeneous, and distributed measurements which focus on the anisotropic physical and gradient scale lengths of aurorae, and discrete sheet-like morphologies. The reconstruction, replication, and weighted replication methodologies all aim to use maximal information from imagery derived precipitation maps to provide geophysical extrapolations of plasma flow maps surrounding auroral arcs. This is achieved by the following extensions to work done by Clayton et al. (2019):

1. Opting for imagery derived Pedersen conductance contour lines, in place of energy flux gradients, as a more natural choice for replicating electric field data.
2. Using a secondary auroral arc boundary to which the plasma flow data are scaled in an attempt to co-locate shorted-out electric fields with enhanced precipitation.
3. Rotating replicated plasma flow data to ensure the zeroth order flow shear definition of auroral arcs.

4. Using the Fourier Representation Of Poisson's Equation technique in enforcing electrostatics.

Figures 7 and 10 demonstrate these improvements. These additional measures ensure that the relative directions between the electric fields and the imagery related gradients are more geophysical, and they represent the next step toward studying auroral arcs that stray from ideal, sheet-like morphologies.

4.2 Cautionary remarks

The Gaussian smoothing of the plasma flow data (referred to in Section 2.2.2) should not be arbitrary. Eq. (1) shows that the gradients in the data track direction directly affect the magnitude of the FAC. The resolution of the optical data (often the limiting resolution) should match the resolution of the plasma flow data in such a way that the Pedersen, Hall conductance gradient, and diverging electric field terms balance in Eq. (1). For example, Figure 8 shows a precipitation and conductance map that have similar minimum structure sizes to that of the resulting plasma flow maps. As a validation check, the area integral of the model calculated FAC map over the region of interest should approximately vanish.

Improvements are being made to all-sky imagery inversions, however. The resolution of optical data were previously limited by the necessity of time averaging or spatial low-pass filtering to suppress CCD noise. At the time of writing, we are exploring the use of translation-equivariant wavelet denoising to suppress noise while preserving high spatial and time resolution, as well as across-arc gradients.

As a further cautionary reminder, the replicated plasma flow interpolation (see Section 2.2.3) needs to be done using cubic or cubic spline methods to ensure a continuity of C^1 or higher. Using linear interpolation results in strong rippling of simulated FAC because of discontinuous first derivatives of the electric field.

5 Conclusions and Applications

Measurements of auroral arc systems can be sparse, heterogeneous, and widely distributed, while ionospheric models generally require continuous top-boundary drivers. We address this challenge by using extensive information from multi-spectral, all-sky imagery. We have outlined three empirical methods for creating electrostatic, spatially continuous, topside ionospheric convection boundary conditions that focus on typical sheet-like discrete auroral arc structures. The main takeaways are as follows:

1. Even for the most basic auroral arc systems, a 1D (latitude) or 2D (latitude-altitude) description can be insufficient and may hide the 3D nature of current closure.
2. When extrapolating ionospheric topside plasma flow data surrounding auroral arcs it is important to scale the data in a way that co-locates the associated shorted-out electric fields with the region of enhanced conductance.
3. Similarly, it is important to rotate the plasma flow data in a way that avoids introducing arbitrary angles between the ionospheric electric field and the conductance gradients.
4. Current flux tubes whose ends are near the FAC inflection line between an upward and downward current sheet can close through Pedersen current at altitudes well above where Pedersen conductivity maximizes.
5. Current flux tubes surrounding auroral arcs can split; a region of FAC inside one downward current sheet can close in two upward current sheets.

It is possible to merge the techniques described in this paper with Lompe (Laundal et al., 2022) to provide even more self-consistency. This could be done directly by using replicated flow maps (with appropriate weighting) and FAC data. Another way would be by adding constraints to Lompe that prioritize solutions with small angles between conductance gradients and flow, and solutions with small products between electric field and conductances to act as step 2 and 3 in Section 2.2.2.

Finding a set of electrostatic auroral conductances, convection flow, and FAC maps that are physical and self-consistent can be fully determined through current continuity. Finding a set that appears in nature, on Earth, and is likely, however, requires a greater understanding of the three-dimensional interplay between these three ingredients. The techniques outlined in this paper can be used to develop a series of data-driven 3D simulations provided by conjunctions like those from the *Swarm-over-Poker-2023* campaign. Conjunctions which include convection flow data provided by EISCAT 3D (Stamm et al., 2021) can also be used in the future using these techniques. Such simulations can be idealized to retain only the fundamental auroral structures (peak precipitation flux, flow shear, arc width, etc.) where the resulting data-*inspired* simulations can be defined by a manageable number of parameters. This parameter space can be strategically explored, gradually straying auroral systems from ideal, sheet-like structure. Understanding the physical mechanisms connecting these various parameters will aid in studying data-driven simulations.

6 Open Research

All 3D simulation data, Isinglass data, imagery inversions, and reconstruction/replication tools are available at `https://rcweb.dartmouth.edu/lynchk`. The data for the Poker Flat DASC are available at `http://optics.gi.alaska.edu/optics/archive`, for AMISR at `https://data.amisr.com/database`, and for the Swarm TII at `https://swarm-diss.eo.esa.int`. The GEMINI source code and documentation is available at `https://github.com/gemini3d`.

Acknowledgments

We thank NASA for funding Jules van Irsel from grant 80NSSC23K1622 through the FINESST program and Dartmouth College for providing internal funding for Phase A of the Auroral Reconstruction CubeSwarm proposal from which a lot of this research stems, and we acknowledge NASA grant 80GSFC21C0009 for the ARCS MIDEX CSR funding. We are grateful for the data providers from the Isinglass rocket team and we acknowledge Isinglass LCAS support from NASA grant NNX14AH07G. The Poker Flat Incoherent Scatter Radar and Digital All-Sky Camera are operated by the SRI International for the National Science Foundation as part of the AMISR program through cooperative agreement AGS-1840962. This work uses version 0302, level 1B data from the Thermal Ion Imagers made possible by the European Space Agency's Swarm Data, Innovation, and Science Cluster. We thank NASA for providing funding for the GEMINI model development from grant 80NSSC24K0126. 3D simulations supporting this work were facilitated by the Discovery cluster at Dartmouth Research Computing and the NASA High-End Computing (HEC) Program through the NASA Advanced Supercomputing (NAS) Division at Ames Research Center. We would like to thank Michael Hirsch, Terry Kovacs, and John Griffin for GEMINI and computational technical support. We also like to thank Meghan Burleigh for her invaluable input in reviewing this manuscript, and Leslie Lamarche and Hayley Clevenger for insightful discussions. Lastly we thank Don Hampton and Leslie Lamarche, along with NSF grant 2329979, for providing support for the *Swarm-over-Poker-2023* campaign.

References

Ahlfors, L. V. (1953). Complex analysis: An introduction to the theory of analytic functions of one complex variable. *New York, London*, *177*.

Amm, O. (1997). Ionospheric elementary current systems in spherical coordinates and their application. *Journal of Geomagnetism and Geoelectricity*, *49*(7), 947-955. doi: 10.5636/jgg.49.947

Archer, W. E., Knudsen, D. J., Burchill, J. K., Jackel, B., Donovan, E., Connors, M., & Juusola, L. (2017). Birkeland current boundary flows. *Journal of Geophysical Research: Space Physics*, *122*(4), 4617-4627. doi: 10.1002/2016JA023789

Bristow, W. A., Hampton, D. L., & Otto, A. (2016). High-spatial-resolution velocity measurements derived using Local Divergence-Free Fitting of SuperDARN observations. *Journal of Geophysical Research: Space Physics*, *121*(2), 1349-1361. doi: 10.1002/2015JA021862

Clayton, R., Burleigh, M., Lynch, K. A., Zettergren, M., Evans, T., Grubbs, G., … Varney, R. (2021). Examining the auroral ionosphere in three dimensions using reconstructed 2D maps of auroral data to drive the 3D GEMINI model. *Journal of Geophysical Research: Space Physics*, *126*(11). doi: 10.1029/2021JA029749

Clayton, R., Lynch, K., Zettergren, M., Burleigh, M., Conde, M., Grubbs, G., … Varney, R. (2019). Two-dimensional maps of in situ ionospheric plasma flow data near auroral arcs using auroral imagery. *Journal of Geophysical Research: Space Physics*, *124*(4), 3036-3056. doi: 10.1029/2018JA026440

Conde, M., Craven, J. D., Immel, T., Hoch, E., Stenbaek-Nielsen, H., Hallinan, T., … Sigwarth, J. (2001). Assimilated observations of thermospheric winds, the aurora, and ionospheric currents over Alaska. *Journal of Geophysical Research: Space Physics*, *106*(A6), 10493-10508. doi: 10.1029/2000JA000135

Cowley, S. W. H. (2000). Magnetosphere-ionosphere interactions: A tutorial review. *Magnetospheric Current Systems, Geophysical Monograph Series*, *118*, 91-106.

Enengl, F., Kotova, D., Jin, Y., Clausen, L. B. N., & Miloch, W. J. (2023). Ionospheric plasma structuring in relation to auroral particle precipitation. *Journal of Space Weather and Space Climate*, *13*. doi: 10.1051/swsc/2022038

Erlandson, R., Lynch, K. A., Samara, M., Anderson, B., Bortnik, J., Burleigh, M., ... Zou, S. (2024). *Auroral Reconstruction CubeSwarm (ARCS).*

Fang, X., Randall, C. E., Lummerzheim, D., Solomon, S. C., Mills, M. J., Marsh, D. R., ... Lu, G. (2008). Electron impact ionization: A new parameterization for 100 eV to 1 MeV electrons. *Journal of Geophysical Research: Space Physics*, *113*(A9). doi: 10.1029/2008JA013384

Fang, X., Randall, C. E., Lummerzheim, D., Wang, W., Lu, G., Solomon, S. C., & Frahm, R. A. (2010). Parameterization of monoenergetic electron impact ionization. *Geophysical Research Letters*, *37*(22). doi: 10.1029/2010GL045406

Fujii, R., Amm, O., Vanhamäki, H., Yoshikawa, A., & Ieda, A. (2012). An application of the finite length Cowling channel model to auroral arcs with longitudinal variations. *Journal of Geophysical Research: Space Physics*, *117*. doi: 10.1029/2012JA017953

Fujii, R., Amm, O., Yoshikawa, A., Ieda, A., & Vanhamäki, H. (2011). Reformulation and energy flow of the Cowling channel. *Journal of Geophysical Research: Space Physics*, *116*(A2). doi: 10.1029/2010JA015989

Grubbs II, G., Michell, R., Samara, M., Hampton, D., Hecht, J., Solomon, S., & Jahn, J. (2018). A comparative study of spectral auroral intensity predictions from multiple electron transport models. *Journal of Geophysical Research: Space Physics*, *123*(1), 993-1005. doi: 10.1002/2017JA025026

Grubbs II, G., Michell, R., Samara, M., Hampton, D., & Jahn, J. (2018). Predicting electron population characteristics in 2-D using multispectral ground-based imaging. *Geophysical Research Letters*, *45*(1), 15-20. doi: 10.1002/2017GL075873

Heinselman, C. J., & Nicolls, M. J. (2008). A Bayesian approach to electric field and E-region neutral wind estimation with the Poker Flat Advanced Modular Incoherent Scatter Radar. *Radio Science*, *43*(5). doi: 10.1029/2007RS003805

Kaeppler, S., Markowski, D. G., Pepper, A. M., Troyer, R., Jaynes, A. N., Varney, R. H., & Hampton, D. (2023). Data-driven empirical conductance relations during auroral precipitation using incoherent scatter radar and all sky imagers. *Journal of Geophysical Research: Space Physics*. doi: 10.1029/2023JA031764

Kamide, Y., Richmond, A. D., & Matsushita, S. (1981). Estimation of ionospheric electric fields, ionospheric currents, and field-aligned currents from ground magnetic records. *Journal of Geophysical Research: Space Physics*, *86*(A2), 801-813. doi: 10.1029/JA086iA02p00801

Kelley, M. C. (2009). *The Earth's ionosphere: Plasma physics and electrodynamics* (2nd ed.). Amsterdam, Netherlands: Academic Press.

Kelly, J., & Heinselman, C. (2009). Initial results from Poker Flat Incoherent Scatter Radar (PFISR). *Journal of Atmospheric and Solar-Terrestrial Physics*, *71*(6), 635. doi: 10.1016/j.jastp.2009.01.009

Khazanov, G. V., Robinson, R. M., Zesta, E., Sibeck, D. G., Chu, M., & Grubbs, G. A. (2018). Impact of precipitating electrons and magnetosphere-ionosphere coupling processes on ionospheric conductance. *Space Weather*, *16*(7), 829-837. doi: 10.1029/2018SW001837

Knudsen, D. J., Burchill, J. K., Buchert, S. C., Eriksson, A. I., Gill, R., Wahlund, J.-E., ... Moffat, B. (2017). Thermal ion imagers and Langmuir probes in the Swarm electric field instruments. *Journal of Geophysical Research: Space Physics*, *122*(2), 2655-2673. doi: 10.1002/2016JA022571

Laundal, K. M., Reistad, J. P., Hatch, S. M., Madelaire, M., Walker, S., Hovland, A. Ø., ... Sorathia, K. A. (2022). Local mapping of polar ionospheric electrodynamics. *Journal of Geophysical Research: Space Physics*, *127*(5). doi: 10.1029/2022JA030356

Lotko, W. (2004). Inductive magnetosphere-ionosphere coupling. *Journal of Atmospheric and Solar-Terrestrial Physics*, *66*(15), 1443-1456. doi: 10.1016/j.jastp.2004.03.027

Lynch, K. A., Erlandson, R., Samara, M., Anderson, B., Bortnik, J., Burleigh, M., ... Zou, S. (2024). *Auroral Reconstruction CubeSwarm (ARCS).*

Lynch, K. A., McManus, E., Gutow, J., Burleigh, M., & Zettergren, M. (2022). An ionospheric conductance gradient driver for subauroral picket fence visible signatures near STEVE events. *Journal of Geophysical Research: Space Physics*, *127*(12). doi: 10.1029/2022JA030863

Mallinckrodt, A. J. (1985). A numerical simulation of auroral ionospheric electrodynamics. *Journal of Geophysical Research: Space Physics*, *90*(A1), 409-417. doi: 10.1029/JA090iA01p00409

Marghitu, O. (2012). Auroral arc electrodynamics: Review and outlook. In *Auroral phenomenology and magnetospheric processes: Earth and other planets* (p. 143-158). American Geophysical Union (AGU). doi: 10.1029/2011GM001189

Nicolls, M. J., Cosgrove, R., & Bahcivan, H. (2014). Estimating the vector electric field using monostatic, multibeam incoherent scatter radar measurements. *Radio Science*, *49*(11), 1124-1139. doi: 10.1002/2014RS005519

Nicolls, M. J., & Heinselman, C. J. (2007). Three-dimensional measurements of traveling ionospheric disturbances with the Poker Flat Incoherent Scatter Radar. *Geophysical Research Letters*, *34*(21). doi: 10.1029/2007GL031506

Richmond, A. D., & Kamide, Y. (1988). Mapping electrodynamic features of the high-latitude ionosphere from localized observations: Technique. *Journal of Geophysical Research: Space Physics*, *93*(A6), 5741-5759. doi: 10.1029/JA093iA06p05741

Robinson, R. M., Vondrak, R. R., Miller, K., Dabbs, T., & Hardy, D. (1987). On calculating ionospheric conductances from the flux and energy of precipitating electrons. *Journal of Geophysical Research: Space Physics*, *92*(A3), 2565-2569. doi: 10.1029/JA092iA03p02565

Ruohoniemi, J. M., Greenwald, R. A., Baker, K. B., Villain, J. P., Hanuise, C., & Kelly, J. (1989). Mapping high-latitude plasma convection with coherent HF radars. *Journal of Geophysical Research: Space Physics*, *94*(A10), 13463-13477. doi: 10.1029/JA094iA10p13463

Seyler, C. E. (1990). A mathematical model of the structure and evolution of small-scale discrete auroral arcs. *Journal of Geophysical Research: Space Physics*, *95*(A10), 17199-17215. doi: 10.1029/JA095iA10p17199

Sobel, I. (2014). An isotropic 3×3 image gradient operator. *Presentation at Stanford A.I. Project 1968*.

Solomon, S. C. (2017). Global modeling of thermospheric airglow in the far ultraviolet. *Journal of Geophysical Research: Space Physics*, *122*(7), 7834-7848. doi: 10.1002/2017JA024314

Stamm, J., Vierinen, J., Urco, J. M., Gustavsson, B., & Chau, J. L. (2021). Radar imaging with EISCAT 3D. *Annales Geophysicae*, *39*(1), 119-134. doi: 10.5194/angeo-39-119-2021

Wang, X., Cai, L., Aikio, A., Vanhamäki, H., Virtanen, I., Zhang, Y., . . . Liu, S.

(2024). Ionospheric conductances due to electron and ion precipitations: A comparison between EISCAT and DMSP estimates. *Journal of Geophysical Research: Space Physics*, *129*(2). doi: 10.1029/2023JA032354

Wolf, R. A. (1975, 01). Ionosphere-magnetosphere coupling. *Space Science Reviews*, *17*(2), 537-562. doi: 10.1007/BF00718584

Yano, Y., & Ebihara, Y. (2021). Three-dimensional closure of field-aligned currents in the polar ionosphere. *Journal of Geophysical Research: Space Physics*, *126*(9). doi: 10.1029/2021JA029421

Zettergren, M., & Snively, J. (2019). Latitude and longitude dependence of ionospheric TEC and magnetic perturbations from infrasonic-acoustic waves generated by strong seismic events. *Geophysical Research Letters*, *46*(3), 1132-1140. doi: 10.1029/2018GL081569

Zettergren, M. D., & Semeter, J. L. (2012). Ionospheric plasma transport and loss in auroral downward current regions. *Journal of Geophysical Research: Space Physics*, *117*(A6). doi: 10.1029/2012JA017637

Zettergren, M. D., & Snively, J. B. (2015). Ionospheric response to infrasonic-acoustic waves generated by natural hazard events. *Journal of Geophysical Research: Space Physics*, *120*(9), 8002-8024. doi: 10.1002/2015JA021116